NONLINEAR MODE COUPLING COEFFICENTS IN EXTRASOLAR HOT JUPITER SYSTEMS WITH NON-SOLAR TYPE HOST STARS

by

NIYOUSHA DAVACHI

Presented to the Faculty of the Graduate School of

The University of Texas at Arlington in Partial Fulfillment

of the Requirements

for the Degree of

MASTER OF SCIENCE IN PHYSICS

THE UNIVERSITY OF TEXAS AT ARLINGTON

December 2021

Acknowledgements

I would like to thank my Supervising Professor, Dr. Nevin Weinberg, for his supportive guidance not only throughout the research process, but also in helping me navigate graduate school. The journey would not have been possible without his support, and I am truly grateful for the opportunity he provided me

I would also like to thank all the members of my Supervising Committee: Dr. Nevin Weinberg, Dr. Sangwook Park, and Dr. Zdzislaw Musielak. I am extremely fortunate that you agreed to be on my committee, and your help and support has made my undergraduate and graduate studies possible.

I would also like to thank all the family and friends who helped and supported me throughout my studies.

December 7, 2021

Abstract

NONLINEAR MODE COUPLING COEFFICENTS IN HOT JUPITER SYSTEMS WITH NON-SOLAR TYPE HOST STARS

Niyousha Davachi, MS

The University of Texas at Arlington, 2021

Supervising Professor: Nevin N. Weinberg

Short period planets tidally excite internal gravity modes within their host star. These excited modes, known collectively as the dynamical tide, dissipate orbital energy and cause the planet's orbit to decay. In hot Jupiter systems, resonantly excited g-modes are driven to such large amplitudes in the stellar core that they nonlinearly excite a sea of secondary modes. These secondary modes can greatly enhance the efficiency of tidal dissipation compared to linear theory predictions and thus significantly increase the rate of orbital decay.

In this thesis we calculate the three-mode coupling coefficients between the excited g-modes of hot Jupiter host stars. These coefficients determine the strength of the nonlinear mode interactions and are thus a crucial quantity needed to determine the rate of nonlinear tidal dissipation. Previous studies only calculated the coupling coefficient in solar-type host stars even though hot Jupiters are observed to orbit a wide range of stellar types. We calculate the coupling coefficients for low- and high-mass main sequence stars that correspond to the full range of observed hot Jupiter hosts (from 0.6 $M_{\odot}$ to 1.6 $M_{\odot}$). We find that the coupling coefficient is sensitive to the mass and age

of the host star, suggesting that some hot Jupiter systems are much more prone to orbital decay than others.

Table of Contents

List of Illustrations

List of Equations

List of Tables

Introduction

The first exoplanet orbiting a sun-like star, 51 Peg b, was detected nearly 30 years ago (Mayor & Queloz, 1995) and the astronomers who discovered it were awarded the Nobel prize in physics in 2019. 51 Peg b has a mass approximately that of Jupiter but an orbital period of only 4 days. Since this first detection, there have been 100s of such hot Jupiters detected (see Figure 1-1 for an artistic rendering of a hot Jupiter; they are hot because they orbit so close to their host star, with temperatures as high as 2300 K). Initially, most hot Jupiters were detected by the radial velocity method, i.e., by measuring the Doppler shift of spectral lines from the host star due to its reflex motion caused by the orbiting planet. However, more recently they have been mostly detected via the transit method (Catalog, 2021). An exoplanet transit happens when a planet crosses its host star along our line-of-sight, causing a periodic dimming of the star (see Figure 1-2). The depth of the detection signal is proportional to the ratio of the cross-sectional area of the planet to that of the star's. Larger planets in closer orbits thus have a higher likelihood of being detected by the transit method.

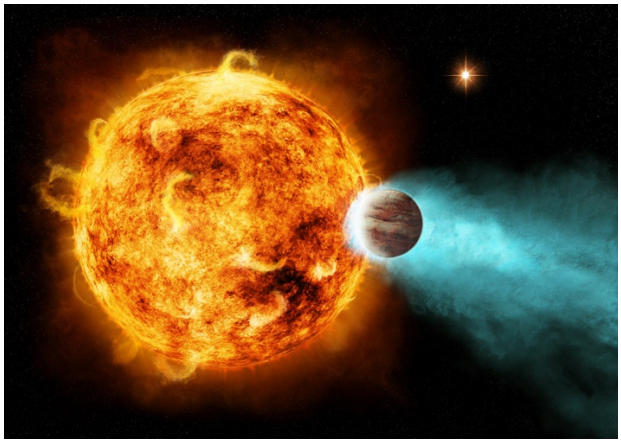

Figure 1-1 Artist's View of a Hot Jupiter System (NASA, 2015)

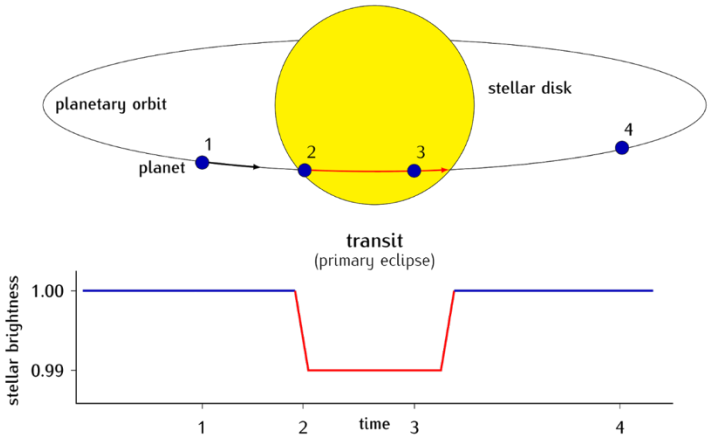

Figure 1-2 Detecting a Planet via Transit Method (Diagrams, 2015)

It is still not understood how hot Jupiters form. They are unlikely to form near their current orbits since the conditions in the protoplanetary disk so close to the protostar are too extreme to form a gas giant. Most theories therefore favor a formation at larger radii (> 1 Astronomical Unit) and a subsequent dynamical process that brings the planet into the short period orbits we see them in today (Dawson & Johnson, 2018). Tides are believed to play a crucial role in the formation process and the subsequent evolution of the orbit. In order to understand the formation, evolution, and ultimate fate of hot Jupiters, we therefore need to understand their tidal interaction with their host stars.

Tidal Dissipation in Hot Jupiter Systems

Stars and close-in hot Jupiters can be considered extended fluid bodies. They are tidally deformed into an ellipsoidal shape due to the variation of the gravitational force across the extent of their bodies (rotation causes them to be oblate too). Dissipation of these large-scale, time-dependent tidal distortions continuously changes the system's orbital and rotational parameters. In particular, tidal dissipation causes the planet's orbit to gradually shrink (i.e., decay) and can ultimately lead to the engulfment of the planet by its host star (Ogilvie, 2014).

In typical hot Jupiter systems, the orbital frequency of the planet Ω is much larger than the spin frequency of the star ω. As we can see in Figure 1-3, in such a situation the tidal bulge in the star lags behind the orbiting planet (this is opposite the Earth-Moon system since there the Earth spins faster than the Moon orbits). As a result, friction is generated between the moving tides and the star (especially in the convective layers). The dissipative nature of the tidal friction causes a loss of orbital energy. Angular momentum is still conserved, though it may be exchanged between the bodies. For a star-planet system with $\Omega \gg \omega$, angular momentum is transferred from the orbit to the stellar spin. The dissipation of orbital energy will cause the planet's orbit to shrink over time, and the transfer of angular momentum will spin up the star (Patra, 2018).

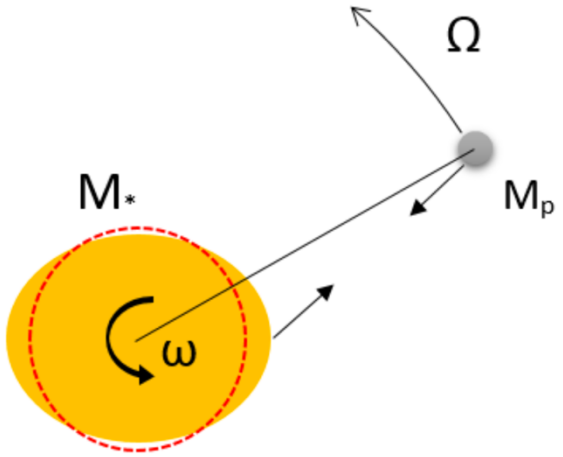

Figure 1-3 Star Tidal Bulge Lags Behind When $\Omega \gg \omega$ (Patra, 2018)

The large-scale, ellipsoidal distortion of the star (and planet) described above is known as the equilibrium tide. Another type of tide that is important in hot Jupiter systems, and is the focus of this thesis, is the dynamical tide. The dynamical tide corresponds to the excitation of internal modes of oscillations (waves) within the star due to the time-dependent tidal perturbation it feels from the planet. Like the equilibrium tide, these waves transfer energy and angular momentum from the orbit to the star. They too can therefore cause the planet's orbit to evolve and decay over time.

Nonlinear Tidal Dissipation

The rate of orbital decay due to the dynamical tide depends on how efficiently the excited modes dissipate their energy. Previous work has shown that resonantly excited modes can reach such large amplitude in the core of the star that they excite secondary modes via nonlinear mode interactions (Barker & Ogilvie, 2010) (Essick & Weinberg,

2016). There can be tens of thousands of such secondary modes excited, many of which have very short wavelengths. The transfer of energy from the orbit to the primary mode and subsequently to the secondary modes can greatly enhance the rate of energy dissipation compared to linear theory estimates (which do not account for the excitation of secondary modes). Nonlinear mode interactions can therefore greatly increase the rate of orbital decay compared to linear theory predictions (Essick & Weinberg, 2016).

As we describe in Chapter 2, how efficiently the primary mode excites secondary modes depends on the strength of their nonlinear coupling. This strength is quantified by a parameter known as the coupling coefficient, which to date has only been calculated for hot Jupiters with sun-like host stars (Weinberg, Arras, Quataert, & Burkart, 2012). However, as we show in the next section, many observed hot Jupiters orbit non-solar type stars. In this thesis, we calculate the coupling coefficients for a wide range of stellar types in order to provide a crucial quantity needed for future studies of nonlinear tidal dissipation in hot Jupiter systems.

Mass distribution of Hot Jupiter Host Stars

In Figure 1-4, we show the observed mass distribution of stars that host hot Jupiters (from exoplanets.org). Although the majority of the observed systems are close to one solar mass, a significant fraction are below and above one solar mass. In this thesis, we calculate coupling coefficients across this full range of stellar masses and their main-sequence evolutionary states. As we will show, the magnitude of the coupling coefficient is sensitive to the internal structure of the star and thus to its mass and age.

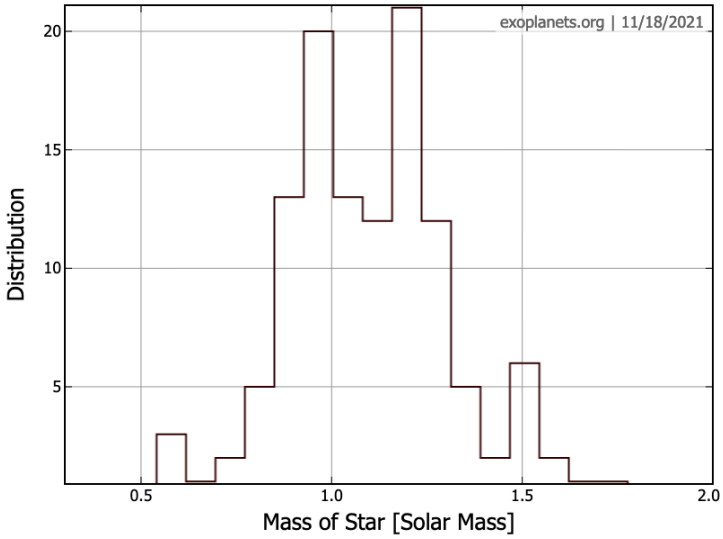

Figure 1-4 Hot Jupiter Host Star Mass Distribution

[redacted]

Methods

In this chapter, we describe the methods we use in our calculations of the coupling coefficients. First, we describe how we construct the background stellar models using the stellar evolution code MESA (Modules for Experiments in Stellar Astrophysics). We then describe how we solve for the linear eigenmodes of these models using the stellar oscillation code GYRE. Finally, we describe the key equations that determine the weakly nonlinear interactions between the stellar oscillation modes, including the integral expression for the coupling coefficient that we need to solve numerically.

Stellar Models

MESA is an open-source code used for calculating the evolution of stars in spherical symmetry (Paxton, et al., 2011) (Paxton, et al., 2019). To match the observed distribution of hot Jupiter host stars shown in Figure 1-4 we used MESA to construct stars with masses of {0.6, 0.8, 1.0, 1.2, 1.4, 1.6} $M_{\odot}$ at different ages on the main sequence, e.g., {1.0, 3.0, 5.0, 7.0, 9.0} Gyr in the case of low mass stars. In total, we constructed 30 distinct stellar models. In Figure 2-1 we show the evolution of the stellar luminosity, radius, and effective temperature as a function of age for the 0.6 $M_{\odot}$and 1.0 $M_{\odot}$ MESA models. We present a MESA inlist sample in Appendix.

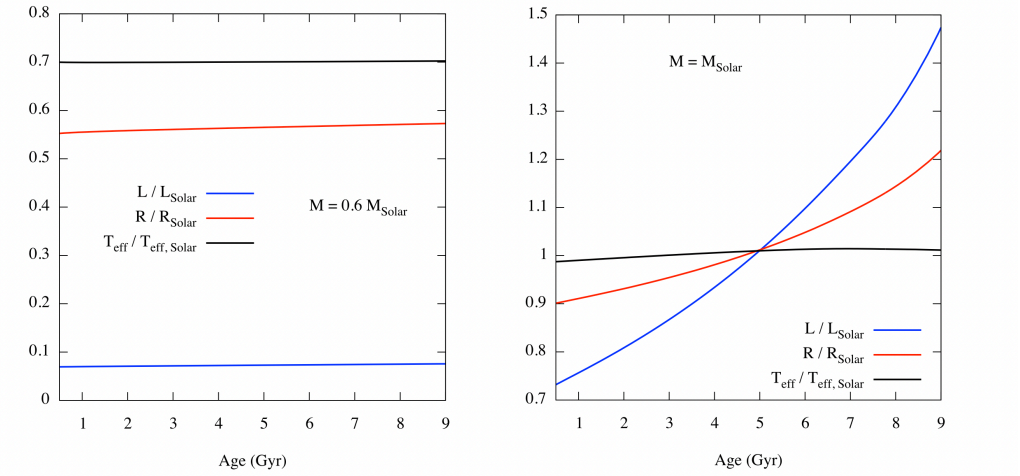

Figure 2-1 Stellar luminosity, radius, and effective temperature (in solar units) as a function of age for MESA models with mass 0.6 $M_{\odot}$ (left panel) and 1.0 $M_{\odot}$ (right panel).

Stellar Eigenfunctions

GYRE (Townsend & Teitler, 2013) is an open-source code that solves for the linear eigenmodes of spherically symmetric stellar models, e.g., those constructed using MESA. When a given stellar model is inputted into GYRE, it calculates the eigenfrequencies and eigenfunctions for the normal oscillation modes of that specific model. We passed our MESA model files to GYRE in order to find oscillation mode solutions. For our desired set of star masses and ages, we determined which dynamical tide modes are most likely to couple well and set the GYRE inlist to find those modes and output their structure to a file. We then use those modes to calculate the coupling coefficients as described below.

As an example, Figure 2-2 shows the radial displacement of a short wavelength g-mode (internal gravity wave) as a function of radius for a solar-type star (1.0 $M_{\odot}$). It is

a short wavelength quadrupolar mode (angular degree l=2) with oscillation period of 5 days. A planet with orbital period twice this value would resonantly excite this mode. We see that the mode steepens as it approaches the center of the star before turning around and decreasing very close to the center. This steepening is due to geometric focusing and we will see that where the displacement is largest contributes most to the coupling coefficient.

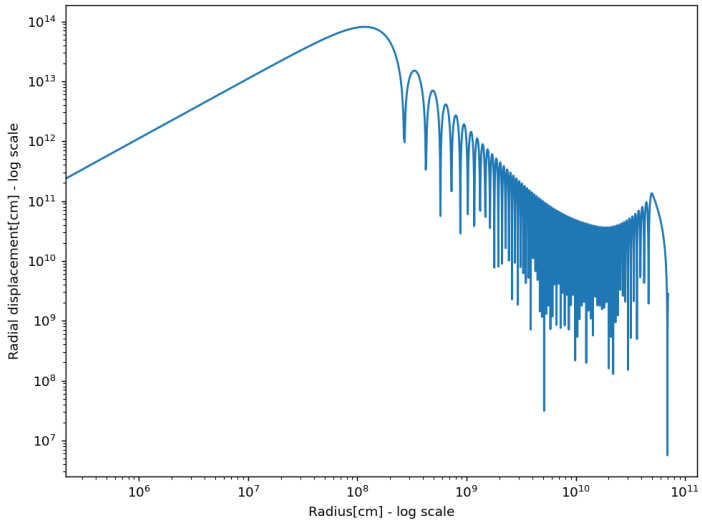

Figure 2-2 Radial displacement of an l=2 eigenfunction of a $1M_{\odot}$ sun-like star.

For comparison, Figure 2-3 shows the radial displacement of an l=2 mode in a more massive star, namely, a $1.6\ M_{\odot}$ star. The image is taken from the star at the age of 1.5 Gyr. We see that the structure of the mode is very different from the mode in the solar-type star. In particular, rather than increasing in amplitude near the core, the displacement decreases exponentially. This is because the core of this more massive star is convective. The restoring force of g-modes is buoyancy and since convection

zones are neutrally buoyant, g-modes are evanescent in these regions, i.e., they do not propagate (Aerts, Christensen-Dalsgaard, & Kurtz, 2010). This is why the exponential decline in displacement starts near a radius of 1e10 cm, which is the top of the convective core. As we will see, this difference between the low and high mass stellar structures and thus eigenfunctions has important implications for the magnitude of the nonlinear coupling coefficients.

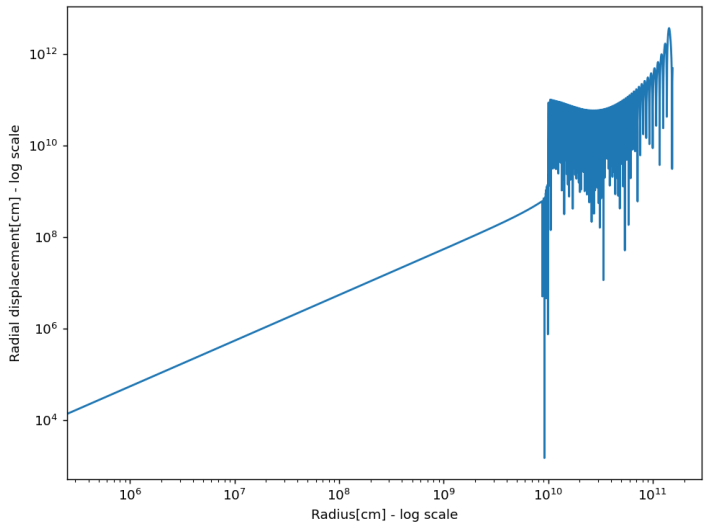

Figure 2-3 Similar to Figure 2-2 except for a $1.6\ M_{\odot}$ star with age 1.5 Gyr.

Another way to understand why the mode structures are so different between the low mass and high mass stars is to look at the profile of the Brunt-Vaisala frequency $N(r)$ (also known as the Brunt frequency and the buoyancy frequency). In regions where $N > 0$ the fluid is buoyant and g-modes propagate. Figure 2-4 shows N^2 for a solar mass star at different ages. We see that it is positive for about the inner 70% of the star and negative for about the outer 30% (we plot the absolute value in order to display it on the

log plot). These correspond, respectively to the radiative and convective regions of the star. Comparing with Figure 2-2, we see that the mode oscillates in the region where $N > 0$ and that the Brunt frequency sets the inner and outer turning points of the mode.

In Figure 2-5 we show the Brunt frequency for a high mass star. We see that now N<0 in the core of the star, where it is convective. Comparing with Figure 2-3, the displacement decreases exponentially precisely where N<0 (note the log vs linear scale in the x-axis of the two plots).

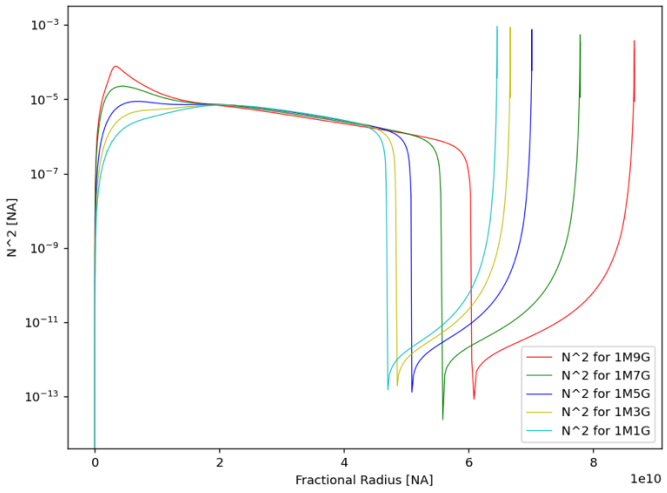

Figure 2-4 Brunt frequency squared for the solar-mass model at different ages

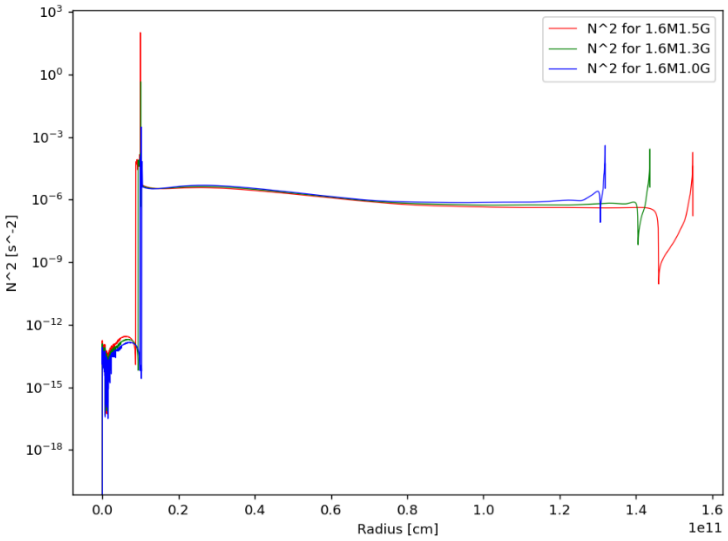

Figure 2-5 Higher Mass Star Brunt Frequency

Non-Linear Amplitude Equations

As described in the introduction, the tide due to a hot Jupiter excites g-modes within the host star. These modes can reach such large amplitude near the center of the star that the linear approximation is not valid (just like Hooke's law for a spring is not valid if the mass attached to the spring is pulled too far) and the modes can nonlinearly excite secondary modes.

We use the formalism developed in WAQB (Weinberg, Arras, Quataert, & Burkart, 2012) for studying the tides in close binary systems in which weakly nonlinear wave interactions are important. The reader should refer to that paper for more in-depth discussions.

The Lagrangian displacement $\boldsymbol{\xi}(\boldsymbol{r}, t)$ of the stellar fluid at position $\boldsymbol{r}$ and time t relative to the unperturbed background gives us the following equation of motion

$$\rho\ddot{\boldsymbol{\xi}} = \boldsymbol{f}_1[\boldsymbol{\xi}] + \boldsymbol{f}_2[\boldsymbol{\xi}, \boldsymbol{\xi}] + \rho \boldsymbol{a}_{tide},$$

Equation 2-1

where ρ is the background density, f_1 and f_2 are the linear and leading-order nonlinear restoring forces,

$$\boldsymbol{a}_{tide} = -\boldsymbol{\nabla} U - (\boldsymbol{\xi}.\boldsymbol{\nabla})\boldsymbol{\nabla} U$$

Equation 2-2

is the tidal acceleration, and U is the tidal potential. We only consider the dominant $l = 2$ tidal harmonic. The displacement $\boldsymbol{\xi}$ is expanded in terms of the eigenfunctions of the star $\boldsymbol{\xi}_{\boldsymbol{\alpha}}$ as follows

$$\begin{bmatrix} \boldsymbol{\xi}(\boldsymbol{r}, t) \\ \partial_t \boldsymbol{\xi}(\boldsymbol{r}, t) \end{bmatrix} = \sum_{\alpha} q_\alpha(t) \begin{bmatrix} \boldsymbol{\xi}_\alpha(\boldsymbol{r}) \\ i\omega_\alpha \boldsymbol{\xi}_\alpha(\boldsymbol{r}) \end{bmatrix}$$

Equation 2-3

where α labels a linear eigenmode with eigenfunction ξ_α, eigenfrequency ω_α, and amplitude $q_\alpha(t)$. Since the eigenfunctions form a complete basis, any displacement $\boldsymbol{\xi}$ can be expanded in this way (similar to the sine/cosine expansion of a Fourier series). This approach to solving a partial differential equation (i.e., Equation 2-1) is sometimes referred to as the method of weighted residuals. There is a freedom in how the eigenmodes are normalized. We normalize them such that

$$E_0 \equiv \frac{GM^2}{R} = 2\omega_\alpha^2 \int d^3\, x \rho \boldsymbol{\xi}_\alpha^* . \boldsymbol{\xi}_\alpha$$

Equation 2-4

With this normalization, a mode with dimensionless amplitude $|q_\alpha| = 1$ has energy E_0 (which is approximately the binding energy of the star – thus, ordinarily $|q_\alpha| \ll 1$). . We

then plug Equation 2-4 into Equation 2-1 and add a linear damping term. Using the orthogonality of eigenmodes leads us to the following equation

$$\dot{q_\alpha} + (i\omega_\alpha + \gamma_\alpha)q_\alpha = i\omega_\alpha \left[U_\alpha(t) + \sum_\beta U^*_{\alpha\beta}(t)q^*_\beta + \sum_{\beta\gamma} \kappa^*_{\alpha\beta\gamma}\, q^*_\beta q^*_\gamma \right]$$

Equation 2-5 Amplitude Equation

where the coefficients

$$U_\alpha(t) = -\frac{1}{E_0}\int d^3x \rho \boldsymbol{\xi}^*_\alpha . \boldsymbol{\nabla} U$$

Equation 2-6

$$U_{\alpha\beta}(t) = -\frac{1}{E_0}\int d^3x \rho \boldsymbol{\xi}_\alpha . (\boldsymbol{\xi}_\beta . \boldsymbol{\nabla})\boldsymbol{\nabla} U$$

Equation 2-7

$$\kappa_{\alpha\beta\gamma} = \frac{1}{E_0}\int d^3x \xi_\alpha . f_2[\xi_\beta, \xi_\gamma]$$

Equation 2-8

The coefficient γ_α is the linear damping rate of the mode, U_α and $U_{\alpha\beta}$ are linear and nonlinear tidal force, and $\kappa_{\alpha\beta\gamma}$ represents the three-mode coupling coefficient. As we can see, $\kappa_{\alpha\beta\gamma}$ is an important quantity needed to determine $q_\alpha(t)$ and we are interested in calculating it for different stellar models. The results of our calculations are presented in Chapter 3.

Note that Equation 2-1 is the amplitude equation for only mode α and that the nonlinear terms on the right-hand side involve sums over other modes β, γ etc. Each of these other modes also satisfy an amplitude equation analogous to Equation 2-1. All the modes are therefore coupled to each other through a set of nonlinear ordinary differential

equations. The solution of these coupled equations determines each modes time-dependent amplitude $q_\alpha(t)$ and thus the energy dissipation $\gamma_\alpha|q_\alpha|^2$ due to each mode. By summing over all the excited modes, the total rate of tidal dissipation can be determined.

Numerically Useful Form for Non-Linear Coupling Coefficient

In this section we provide details on how we calculate the coupling coefficients $\kappa_{\alpha\beta\gamma}$. Due to the oscillatory nature of the modes, the integral needs to be done with great care to avoid numerical error. WAQB derive a form for the integral that is numerically useful and minimizes sources of numerical error. The expression derived there and which we use in order to numerically integrate $\kappa_{\alpha\beta\gamma}$ (here written as κ_{abc}) for the different MESA models, is as follows.

$$\kappa_{abc} = \frac{1}{2E_0}\int dr\,\Big[T\,r^2 p\left\{\Gamma_1(\Gamma_1+1)+\frac{\partial\Gamma_1}{\partial\ln\rho}\right\}\boldsymbol{\nabla}.\boldsymbol{a}\boldsymbol{\nabla}.\boldsymbol{b}\boldsymbol{\nabla}.\boldsymbol{c}$$

$$+ Tr\rho\Gamma_1\,(\boldsymbol{\nabla}.\boldsymbol{a}\boldsymbol{\nabla}.\boldsymbol{c}\{b_h\Lambda_b^2-4b_r\}+\boldsymbol{\nabla}.\boldsymbol{a}\boldsymbol{\nabla}.\boldsymbol{b}\{c_h\Lambda_c^2-4c_r\}$$

$$+\ \boldsymbol{\nabla}.\boldsymbol{b}\boldsymbol{\nabla}.\boldsymbol{c}\{a_h\Lambda_a^2-4a_r\})+T\frac{d\rho}{d\ln r}\left(4g+r\frac{dg}{dr}\right)a_r b_r\,c_r$$

$$+T\rho r\left(4g+r\frac{dg}{dr}\right)\{\boldsymbol{\nabla}.\boldsymbol{a}b_r c_r+\boldsymbol{\nabla}.\boldsymbol{b}c_r a_r+\boldsymbol{\nabla}.\boldsymbol{c}a_r b_r\}$$

$$-\rho r a_h b_h c_h\{\omega_a^2 G_a+\omega_b^2 G_b+\omega_c^2 G_c\}$$

$$-\rho r a_r b_h c_h\{(\omega_a^2-3\omega_b^2-3\omega_c^2)F_a-2(\omega_b^2 F_b+\omega_c^2 F_c)\}$$

$$-\rho r b_r c_h a_h\{(\omega_b^2-3\omega_c^2-3\omega_a^2)F_b-2(\omega_c^2 F_c+\omega_a^2 F_a)\}$$

$$-\rho r c_r a_h b_h\{(\omega_c^2-3\omega_a^2-3\omega_b^2)F_c-2(\omega_a^2 F_a+\omega_b^2 F_b)\}$$

$$+\rho r a_h b_r c_r\{\omega_b^2 F_b+\omega_c^2 F_c-6\omega_a^2 T\}$$

$$+\rho r b_h c_r a_r\{\omega_c^2 F_c+\omega_a^2 F_a-6\omega_b^2 T\}$$

$$+\rho r c_h a_r b_r\{\omega_a^2 F_a+\omega_b^2 F_b-6\omega_c^2 T\}$$

$$+\rho\left\{\frac{d\ln\rho}{d\ln r}a_r b_r+r(a_r\boldsymbol{\nabla}.\boldsymbol{b}+b_r\boldsymbol{\nabla}.\boldsymbol{a})\right\}\left(r\frac{d\delta\phi_c}{dr}+2\delta\phi_c\right)T$$

$$+\rho\left\{\frac{d\ln\rho}{d\ln r}a_r c_r+r(a_r\boldsymbol{\nabla}.\mathbf{c}+c_r\boldsymbol{\nabla}.\boldsymbol{a})\right\}\left(r\frac{d\delta\phi_b}{dr}+2\delta\phi_b\right)T$$

$$+\rho\left\{\frac{d\ln\rho}{d\ln r}b_r c_r+r(b_r\boldsymbol{\nabla}.\boldsymbol{c}+c_r\boldsymbol{\nabla}.\boldsymbol{b})\right\}\left(r\frac{d\delta\phi_a}{dr}+2\delta\phi_a\right)T\Big]$$

Equation 2-9

Here p is the background pressure ρ is the background density, g is the gravitational acceleration, ω_a is the eigenfrequency of mode a, a_r and a_h are the radial and horizontal Lagrangian displacements, and ϕ_a is the Eulerian perturbation to the gravitational potential (and similarly for modes b and c). The term T is an angular integral over triple products of the spherical harmonics Y_a. It can be reduced to an expression involving the Wigner $3-j$ symbols

$$T \equiv \int d\Omega\, Y_a Y_b\, Y_c =$$

$$\left[\frac{(2l_a+1)(2l_b+1)(2l_c+1)}{4\pi}\right]^{1/2} \begin{pmatrix} l_a & l_b & l_c \\ m_a & m_b & m_c \end{pmatrix} \begin{pmatrix} l_a & l_b & l_c \\ 0 & 0 & 0 \end{pmatrix}$$

Equation 2-10

where the l_a etc. are the angular degree of the modes and the last two terms are the Wigner $3-j$ symbols (not matrices) which we calculate using a publicly available python function. The F and G parameters in

Equation 2-9 can be written in terms of T as

$$F_a \equiv \frac{T}{2}\,(\Lambda_b^2 + \Lambda_c^2 - \Lambda_a^2)$$

Equation 2-11

$$G_a \equiv \frac{T}{4}\,[\Lambda_a^4 - (\Lambda_b^2 - \Lambda_c^2)^2]$$

Equation 2-12

where $\Lambda_a^2 = l_a(l_a+1)$. The modes only couple if they satisfy the angular selection rules $|l_a - l_b| \le l_a \le l_b + l_c$ with $l_a + l_b + l_c$ even and $m_a + m_b + m_c = 0$,

where m is the azimuthal order of the mode. These selection rules ensure angular momentum conservation of the mode interactions.

[redacted]

Results

In this chapter, we present our calculations of the nonlinear coupling coefficients. We first present our results for the case of $1.0\ M_{\odot}$ stars at different ages. We describe the steps of that calculation in detail. We then show our results for the case of both lower mass and higher mass main sequence stars.

Solar Mass Stars

Kappa Results

We use MESA to construct $1.0\ M_{\odot}$ stellar models at different ages; specifically, at $\{1,3,5,7,9\}$ Gyr one. We then feed each MESA model to the oscillation code Gyre to obtain the g-modes needed for the coupling coefficient (i.e., kappa) calculation.

In more detail, we start by extracting each of the variables needed for our kappa calculation shown in

Equation 2-9. Our code reads through MESA and Gyre files and loads all the needed variables. We convert some of the variables of Gyre to our choice of units. We then use the python interpolate package to interpolate all the variables across radius (using cubic spline). This ensures we have sufficient resolution to compute the kappa integral of

Equation 2-9, which as we will show oscillates rapidly in radius. After all the required variables are loaded into our code, we use the python integration package to numerically compute kappa.

To do the integration, we need to select three g-modes. One mode is the parent and the other two are the daughter modes it excites. Since the tide is quadrupolar ($l = 2$) it most strongly excites $l = 2$ parent modes. We therefore have Gyre return $l = 2$ g-modes at the specific periods detailed below. By the angular selection rules, such a parent can couple to $l = 2$ daughter modes. We chose daughters with frequency near half the parent frequency (twice its period) since such triplets are most likely to be unstable to three-mode coupling. We took all three modes to have $m = 0$. Different values of m would only slightly change the results and moreover their kappa can be determined from our results by scaling to different values of the angular integral T. Figure 3-1 shows the

kappa integrand $\frac{d\kappa}{dr}$ of

Equation 2-9 of a sun-like star ($1.0\ M_{\odot}$ and age of 5 Gyr). For this triplet of g-modes, the parent has a period very close to five days, and the daughters have periods very close to ten days (slight differences in their periods yield similar results). We see that the integrand is highly oscillatory and that it peaks near the center of the star. It peaks there because that is where the mode amplitudes peak (see Figure 2-2) and therefore that is where the modes are most nonlinear and where their nonlinear coupling is strongest.

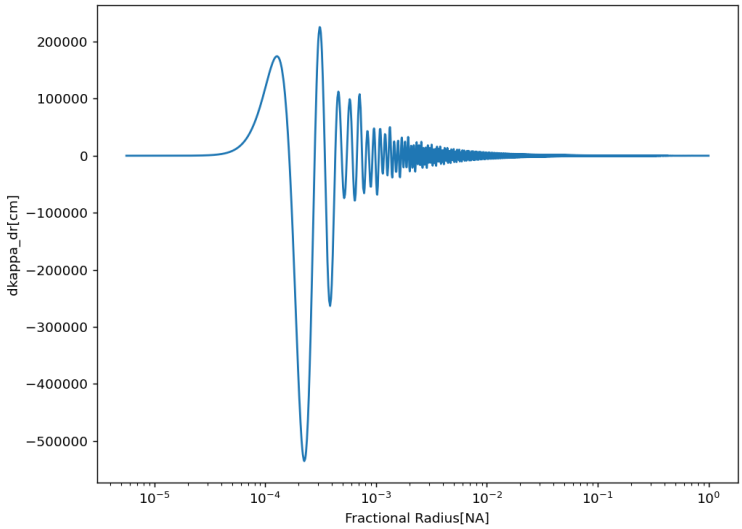

Figure 3-1 Kappa integrand $\frac{d\kappa}{dr}$ (

Equation 2-9) as a function of fractional radius for a sun-like star

For the case of a sun-like star, we used Gyre to find $l = 2$ g-mode parents with periods of 1, 2, 3, 4, 5 days and then find the corresponding $l = 2$ g-mode daughters (those with periods close to twice the parent's). Such parents are resonant with the tidal driving from a planet at orbital period 2, 4, 6, 8, 10 days, respectively. The result of integrating

Equation 2-9 for each if these triplets is shown in Figure 3-2. We see that kappa increases significantly with increasing parent mode period. This is because at longer periods, the parent penetrates closer to the center of the star and its peak amplitude is therefore larger.

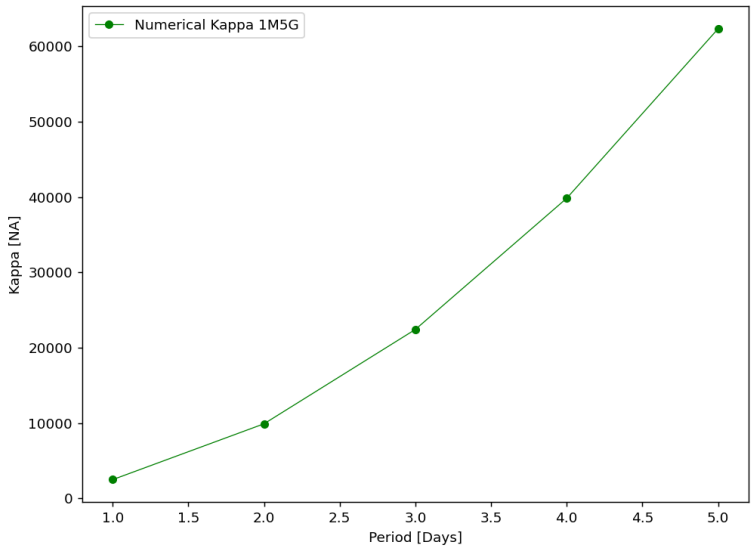

Figure 3-2 Kappa for a sun-like star as a function of parent mode period

Power-law fit for kappa

In Figure 3-3 we show the same result on a log-log plot (blue line). We see that kappa very nearly follows a power-law with period, increasing as period-squared. Our result is in good agreements with the previous results for a sun-like star (Weinberg, Arras, Quataert, & Burkart, 2012):

$$\kappa_{\alpha\beta\gamma} \simeq 2 \times 10^3 \left(\frac{T}{0.2}\right)\left(\frac{P_\alpha}{1\ day}\right)^2$$

Equation 3-1

where P_α is the period of the parent mode and $T \approx 0.1 - 1$ is the angular integral whose exact value depends on each mode's l and m.

The other lines in Figure 3-3 show our kappa calculation for $1.0M_{\odot}$ stars of different ages. We see that to a very good approximation, kappa increases as P^2 in all these stellar models as well.[1] The only difference is the overall magnitude of kappa. We call this overall magnitude scale κ_0 and note that in the case of a sun-like star $\kappa_0 = 2 \times 10^3$ (see Equation 3-1). From the plot, we see that as the star evolves, κ_0 increases. This is because as the star evolves, the core contracts slightly and the buoyancy frequency increases (Figure 2-4). As a result, a parent mode of a given period penetrates closer to the center of the star and its peak amplitude, and hence degree of nonlinearity, increases.

In Table 3-1 we give the numerical value of κ_0 found in our fits for each of the solar mass models shown in Figure 3-3. We display these results on a plot of stellar mass versus stellar age in Figure 3-4. By plotting it this way, we can compare how κ_0 varies with not only the age of the star but also with its mass. We will consider the low mass stars shown in Figure 3-4 in the next section. First, we discuss how we determine the numerical accuracy of our kappa calculations.

[1] There is a slight deviation from this trend for the 9 Gyr model at 5 days. However, this is a numerical artifact due to difficulties integrating modes with extremely short wavelengths (with over 1000 radial nodes through the star). We discuss numerical errors later in the section.

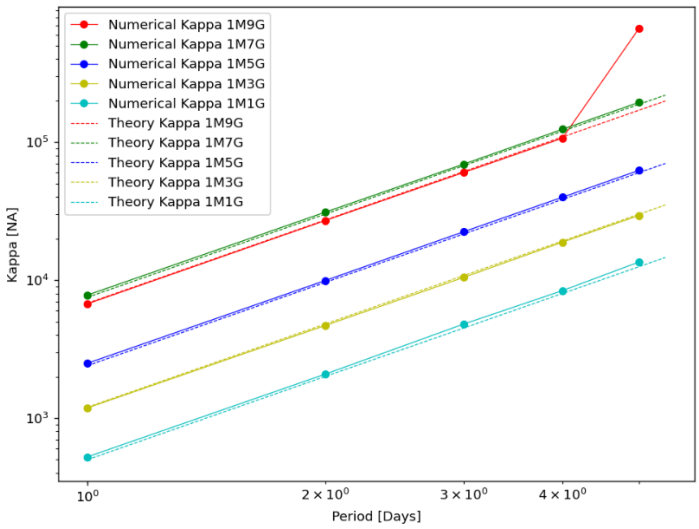

Figure 3-3 Power-law fit (lines) to numerically computed kappa (points) for $1.0M_{\odot}$ stars of different ages.

Age	Mass ($M_{\odot}$)	Numerical κ_0	Theoretical κ_0
9 G	1	6800	NA
7 G	1	7500	NA
5 G	1	2400	2000
3 G	1	1200	NA
1 G	1	500	NA

Table 3-1 Solar Mass κ_0 Values

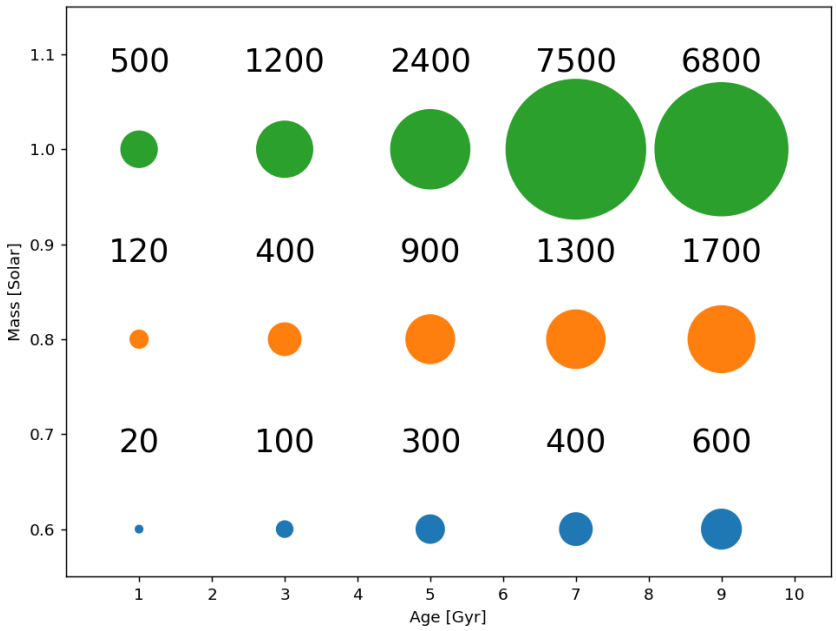

Figure 3-4 The value of κ_0 as a function of stellar mass and age for stars at and below a solar mass.

Error Analysis

In order to carry out the nonlinear coupling coefficient integration, we used a python package called $integrate.quad$ (SciPy, n.d.). This package returns the integration result and an estimate of the numerical error. In addition, it gives us the option to pick the level of integral limit, which is a variable that gives the integration more accuracy by cutting it into more integration areas.

Figure 3-5 shows kappa (points) and its error (error bars) as a function of the python integration limit parameter for the case of a sun-like star. We see that the kappa values are very consistent regardless of the limit we have chosen for the integration as long as we set it to be greater than about 50. This implies that we are obtaining

numerically converged results. We picked a limit value around 120 for different cases as that is a number that consistently generated the smallest error and the most stable integration result as we will see in future plots within chapter 3.

Figure 3-6 shows the same error analysis for a solar mass star at the age of 9 Gyr. The error is noticeably more erratic, suggesting that the spurious point at 9 Gyr shown in Figure 3-3 is affected by numerical error (see Footnote 1).

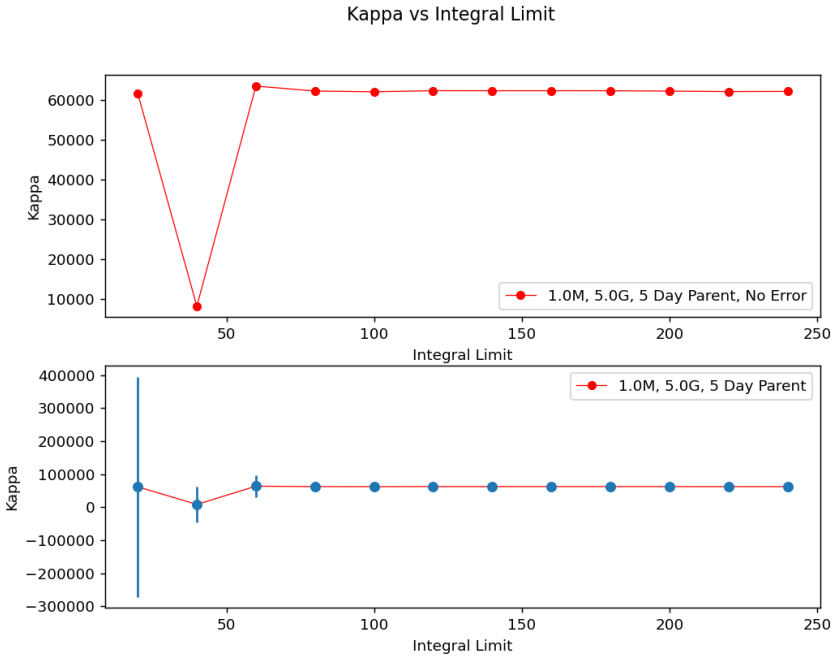

Figure 3-5 Error analysis for a sun-like star. The top panel shows just kappa as a function of the integral limit parameter in python's integrate function while the bottom panel shows kappa with error bars.

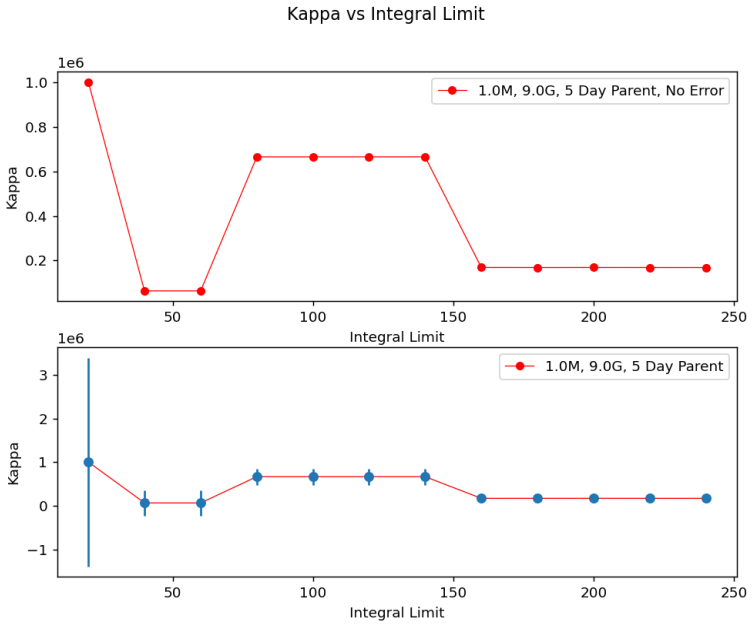

Figure 3-6 Similar to Figure 3-5 but at an age of 9 Gyrs

Lower Mass Stars

In this section, we present our results for the case of lower mass main sequence stars. The calculations and the process of obtaining these results is exactly the same as what we described in the solar mass stars section. We first present our kappa results and fits followed the error analysis.

Kappa Results

We used MESA to generate stellar models with masses of $0.6M_{\odot}$ and $0.8M_{\odot}$ at different ages along the main sequence. As an example, Figure 3-7 shows the kappa

integrand $\frac{d\kappa}{dr}$ as a function of radius for a $0.6M_{\odot}$ at 5 Gyrs and Figure 3-8 shows kappa as a function of period for the same model (compare with Figure 3-1 and Figure 3-2).

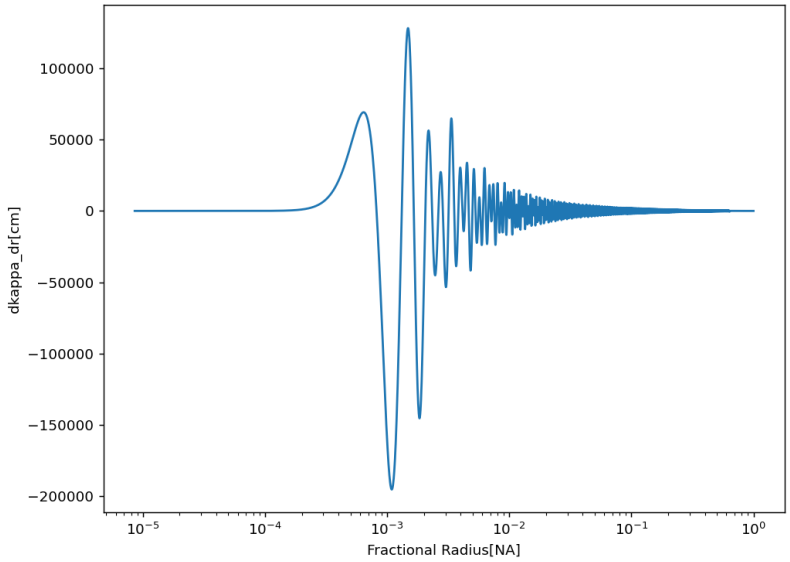

Figure 3-7 Kappa integrand $\frac{d\kappa}{dr}$ as a function of fraction radius for a $0.6M_{\odot}$ star at 5 Gyr.

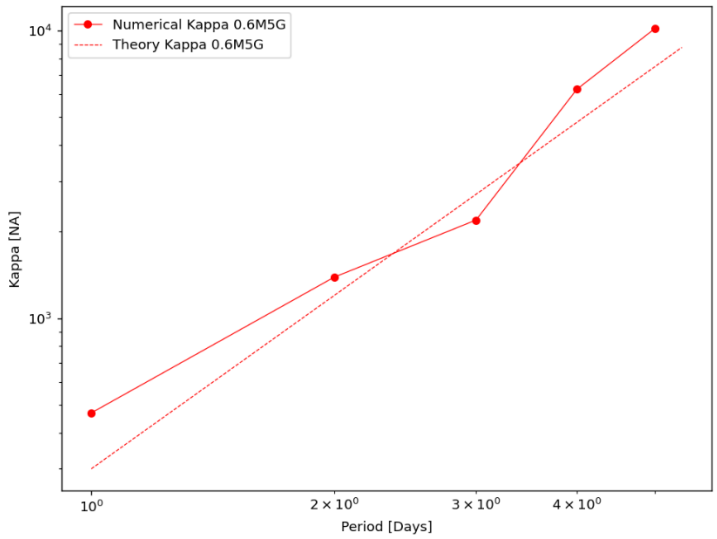

Figure 3-8 κ_0 vs parent mode period for the $0.6M_{\odot}$ model at 5 Gyr.

As we can see in Figure 3-8, the lower mass main sequence star shows a similar trend as the solar-mass star in that kappa increases significantly with increasing period. However, unlike the solar mass case, the trend does not perfectly follow a P^2 power-law slope anymore. This is a behavior we saw in all the lower mass plots we created, and we will look deeper into them in the next section.

Power-law fit for kappa

In this section, we present our stack plot of all the lower mass κ_0 values we calculated. As we can see in the following plot, these stars do not perfectly follow the P^2 rule for kappa vs period. However, except for the youngest model at 1Gyr, it approximately follows a P^2 trend.

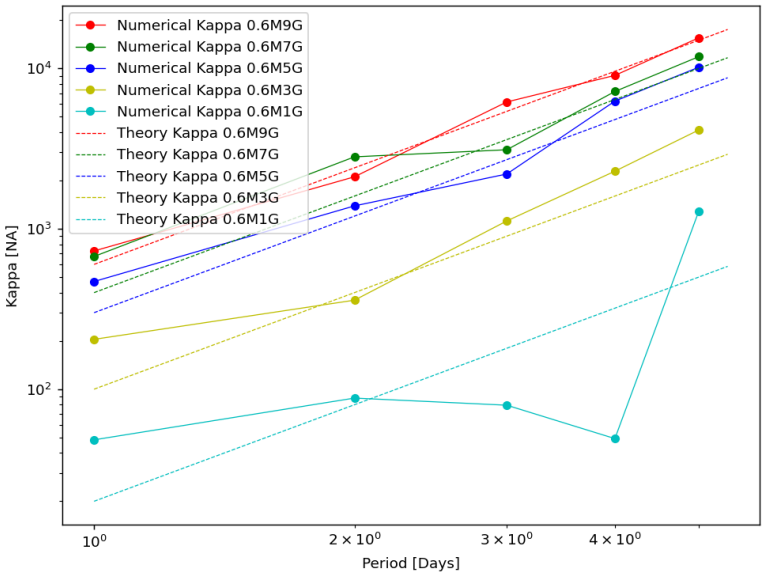

Figure 3-9 kappa vs parent mode period for the $0.6M_{\odot}$ model at different ages.

In Figure 3-4 we show the best fit values of κ_0 for the $0.6M_{\odot}$ and $0.8M_{\odot}$ models at different ages. We see that κ_0 decreases with decreasing stellar mass. This is because lower mass stars have smaller buoyancy frequencies in the core and therefore the parent modes at a given period do not have as a large a peak amplitude.

Error Analysis

As we did in the solar-mass case, in this section, we look at a $0.6M_{\odot}$ at different ages to see the effects of varying the integral limit parameter on the final value of our calculated κ_0. Figure 3-10 shows the result for the 5 Gyr old model. We see that if we

set the integral limit value between 125 and 200, we obtain consistent values for kappa. Figure 3-11 shows the result for the 9 Gyr old model Again we see that for integral limit values above 100 the results are very consistent.

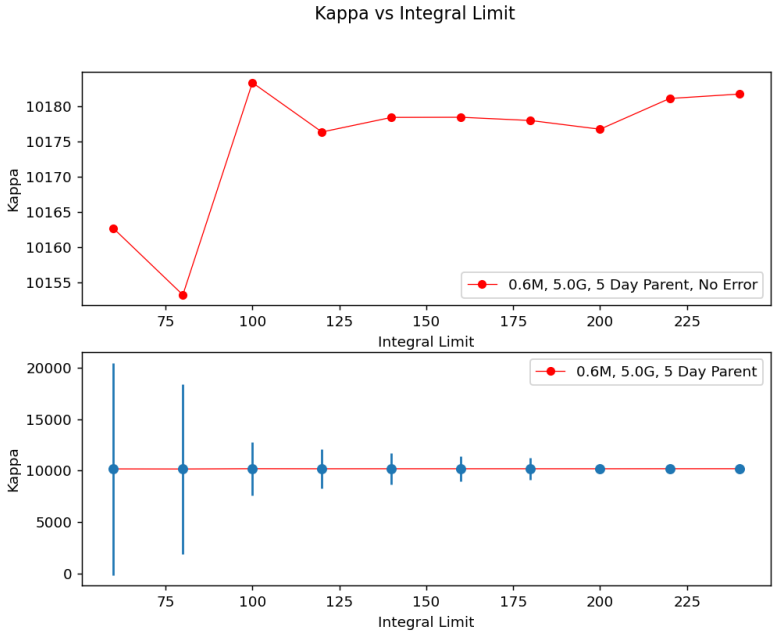

Figure 3-10 Error analysis for the $0.6M_{\odot}$ model at 5 Gyr.

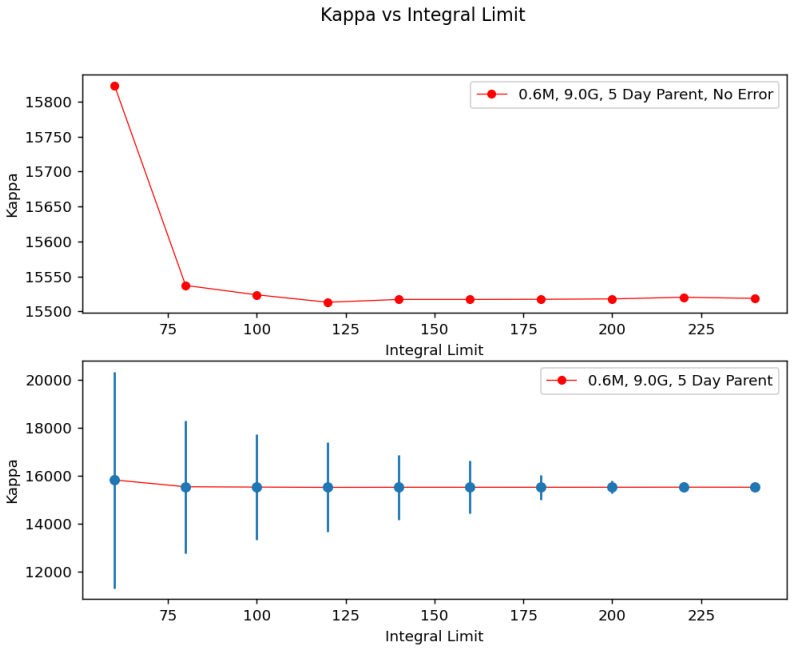

Figure 3-11 Error analysis for the $0.6M_{\odot}$ model at 9 Gyr.

Higher Mass Stars

In addition to solar mass and lower mass stars, we also calculated kappa analysis for higher mass stars that match the range observed to host hot Jupiters. Specifically, we used MESA to construct $1.2M_{\odot}$, $1.4M_{\odot}$, and $1.6M_{\odot}$ models at different ages all along the main sequence. In the next subsection we will describe the kappa results for a single case, followed by general results in future subsections.

Kappa Results

Here we present our results for the case of a $1.6\ M_{\odot}$ at the age of 1.3 Gyr. Figure 3-12 shows the kappa integrand $\frac{d\kappa}{dr}$ as a function of radius. We see the result looks very

different from the corresponding plots from the low mass stars (e.g., Figure 3-7). In particular, although the integrand again steepens towards the center of the star, rather than peak at small radii, the integrand vanishes in the inner $\approx 10\%$ of the star's radius. This is because the core is convective at these radii and the displacement of g-modes are evanescent in convection zones (see Figure 2-4 and Figure 2-5).

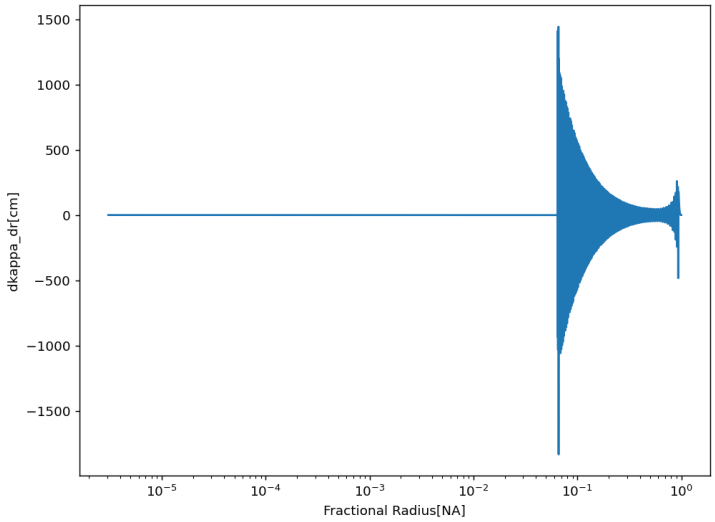

Figure 3-12 Kappa integrand $\frac{d\kappa}{dr}$ as a function of fraction radius for a $1.6M_{\odot}$ star at 1.3 Gyr.

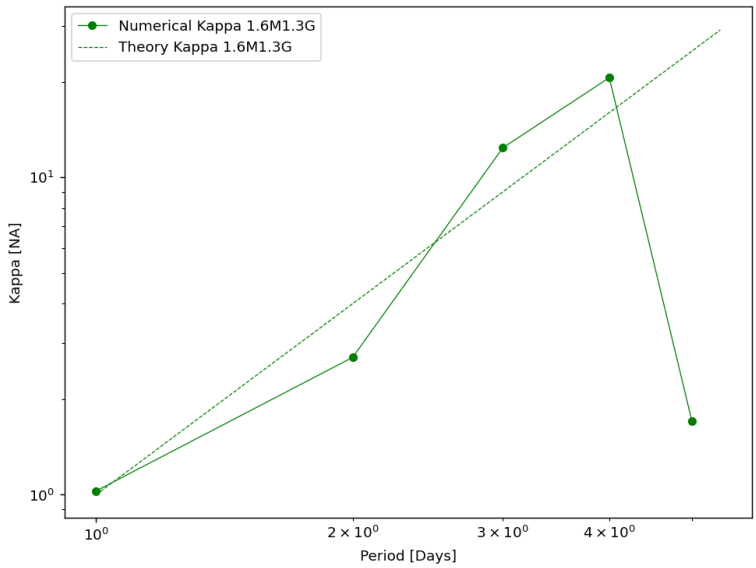

Figure 3-13 kappa vs period for a $1.6\ M_{\odot}$ model a 1.3 Gyr

As we can see in Figure 3-13, the trend of kappa vs period for the $1.6\ M_{\odot}$ model is different compared to solar and lower mass stars as it does not increase as a power-law with period. Figure 3-14 shows kappa vs period for the $1.2\ M_{\odot}$ at different ages and again we see it does not follow a power law but instead increases very little with period and fluctuates somewhat in value. For comparison, the P^2 fit is added, but we can see they do not follow that trend.

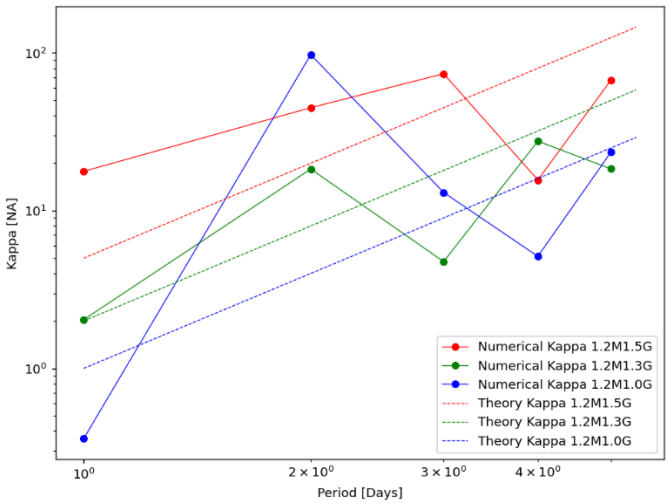

Figure 3-14 kappa vs parent mode period for the $1.2M_{\odot}$ model at different ages.

Although kappa does not follow the the P^2 trend in high mass stars, for the purpose of comparing our calculation to the results for the low mass stars, in Figure 3-15 we show the value kappa for each stellar model averaged over the period range 1.0 to 5.0 days. Comparing this to the corresponding plot for low mass stars shown (Figure 3-4), we see that kappa is much smaller for high mass stars (kappa is on the order of 10 in high mass stars compared to 100-1000 in low mass stars). In addition, kappa does not necessarily increase with mass or age, unlike in the low mass stars. These differences arise because the g-modes are evanescent in the convective core. Thus, the modes are not nearly as nonlinear, and their nonlinear coupling coefficients kappa are much smaller.

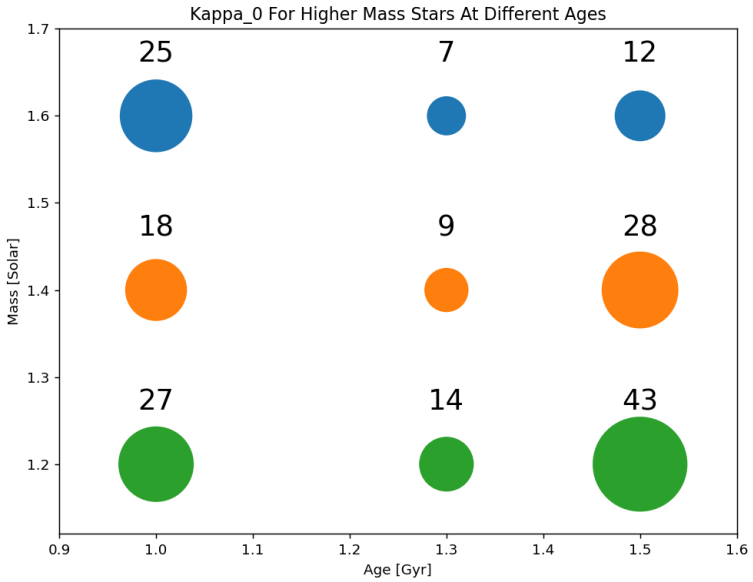

Figure 3-15 The value of the average kappa as a function of stellar mass and age for stars above a solar mass on the main sequence.

Error Analysis

As we did in the solar-mass and low mass cases, in this section, we look at varying the integral limit parameter of the python integrate package affects the calculated value of kappa. As we can see in Figure 3-16, Figure 3-17, Figure 3-18, and Figure 3-19 the calculated kappa values for the high mass models are nearly constant with the integral limit as long as it is set to a sufficiently large value (>100). This suggests we are obtaining numerically convergent results.

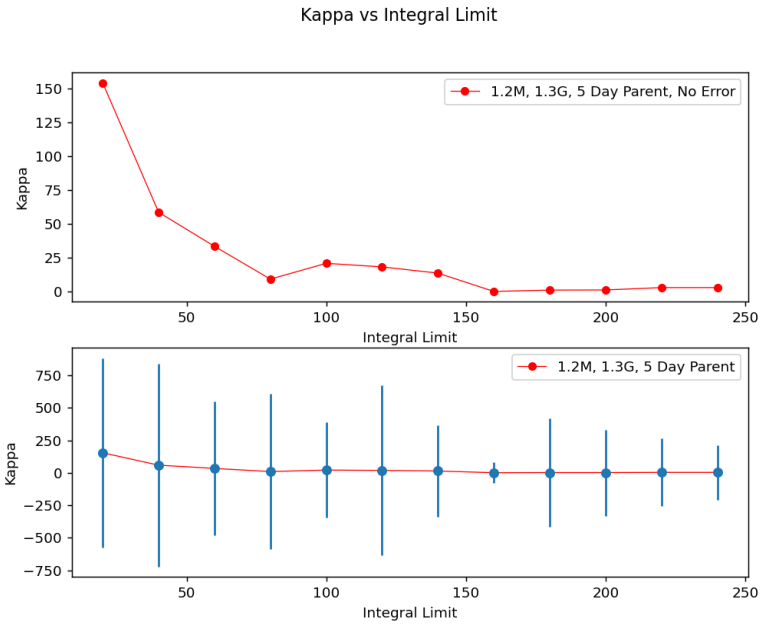

Figure 3-16 Error Analysis for a $1.2\ M_{\odot}$ at Age 1.3 Giga Years

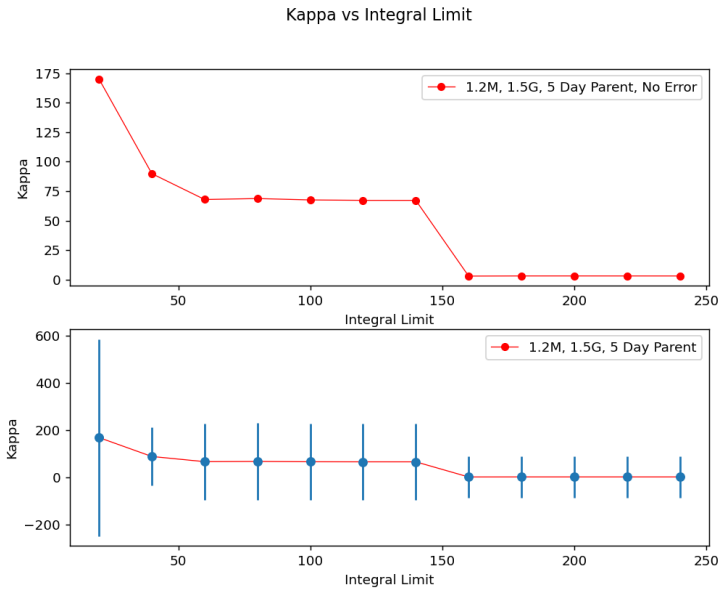

Figure 3-17 Error Analysis for a $1.2\ M_{\odot}$ at Age 1.5 Giga Years

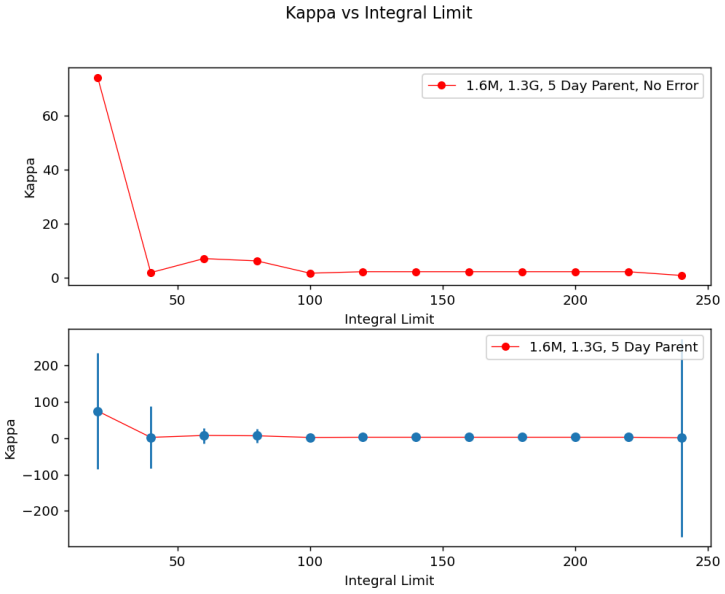

Figure 3-18 Error Analysis for a $1.6\ M_{\odot}$ at The Age of 1.3 Giga Years

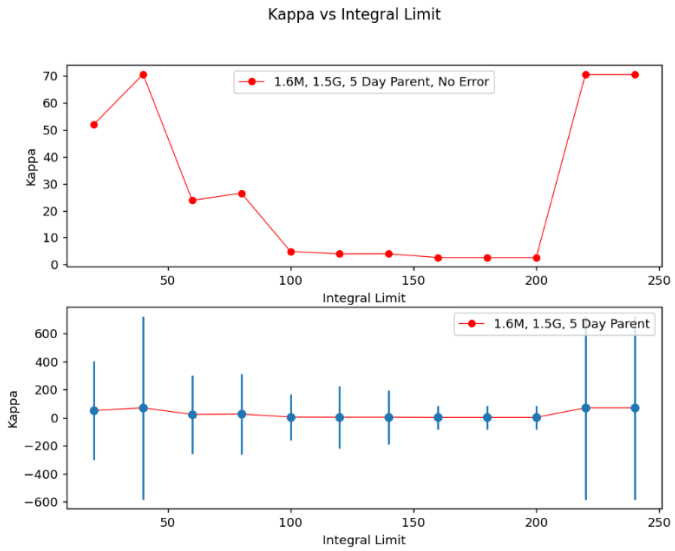

Figure 3-19 Error Analysis for a $1.6\ M_{\odot}$ at the Age of 1.5 Giga Years

Conclusions

In this thesis, we presented the calculation of the nonlinear coupling coefficient of g-modes excited in hot Jupiter host stars. The nonlinear excitation of such modes in the star dissipates the orbital energy, causing the gradual decay of the orbit of hot Jupiters. Understanding the efficiency of this process is important for our understanding of the evolution and fate of hot Jupiter systems.

Previous calculations in the literature only considered the coupling coefficient in hot Jupiter systems with sun-like stars ($1.0 M_{\odot}$ and 4.6 Gyr). However, hot Jupiters are observed to orbit a range of stellar types (Figure 1-4). This thesis addresses this shortcoming by calculating kappa for stars with mass between $0.6 M_{\odot}$ to $1.6 M_{\odot}$ at different ages along the main sequence, in order to better match the full range of stars observed with hot Jupiter companions.

Our results showed that kappa for solar mass and low mass models follows (or very nearly follow) a quadratic trend with orbital period. Moreover, kappa was found to increase with increasing stellar age. By contrast, we found that high mass stars (above a solar mass) show no such a trend with orbital period or age. In addition, we showed that high mass stars have significantly smaller kappa values due to differences in their internal structure (specifically, the presence of a convective core).

Our calculations provide a crucial ingredient for determining the efficiency of tidal dissipation in hot Jupiter host stars and solve for their orbital evolution. Using our kappa results, the next step would be to solve the amplitude equation (Equation 2-5) for the network of nonlinear coupled modes. Such a calculation was previously only done for hot

Jupiters hosting solar type stars (Essick & Weinberg, 2016). With our kappa calculations, such a calculation can now be done for hot Jupiters with non-solar type hosts.

Our results suggest that nonlinear dissipation might be important for lower mass and solar mass stars given that we found they have large kappa. By contrast, nonlinear dissipation is less likely to be important in high mass stars given that we found they have small kappa. This suggests that low mass systems might be much more likely to undergo rapid orbital decay. To confirm this, future studies are needed.

References

Aerts, C., Christensen-Dalsgaard, J., & Kurtz, D. (2010). *Asteroseismology.* Springer.

Barker, A. J., & Ogilvie, G. l. (2010). *Monthly Notices of the Royal Astronomical Society, 404*(4), 1849-1868.

Catalog, E. (2021, November 23). *Exoplanet Catalog*. (Exoplanet Catalog) Retrieved November 2021, from http://exoplanet.eu/catalog/

Dawson, R. l., & Johnson, J. A. (2018). Origins of Hot Jupiters. *Annual Review of Astronomy and Astrophysics, 56*, 175-221.

Diagrams, E. (2015, July 19). *Exoplanet Diagrams*. (Exoplanet Diagrams) Retrieved November 2021, from http://exoplanet-diagrams.blogspot.com/2015/07/the-transit-method.html

Essick, R., & Weinberg, N. N. (2016). Orbital Decay of Hot Jupiters Due to Nonlinear Tidal Dissipation Within Solar-type Hosts. *The Astrophysical Journal, 816*(1), 18.

Mayor, M., & Queloz, D. (1995). A Jupiter-mass companion to a solar-type star. *Nature, 378*(6555), 355-359.

NASA. (2015, October 1). *NASA Exoplanet*. (NASA) Retrieved November 2021, from https://exoplanets.nasa.gov/news/222/threes-company-k2-discovery-shows-hot-jupiter-has-two-planet-friends/

Ogilvie, G. l. (2014). Tidal Dissipation in Stars and Giant Planets. *Annual Review of Astronomy and Astrophysics, 52*, 171-210.

Patra, K. C. (2018). *The Search for Orbital Decay in Hot Jupiters.* Massachusetts: MIT.

Paxton, B., Bildsten, L., Dotter, A., Herwig, F., Lesaffre, P., & Timmes, F. (2011). Modules for Experiments in Stellar Astrophysics (MESA). *The Astrophysical Journal Supplement, 192*(1), 3.

Paxton, B., Smolec, R., Schwab, J., Gautschy, A., Bildsten, L., Cantiello, M., . . . Timmes, F. (2019). Modules for Experiments in Stellar Astrophysics (MESA): Pulsating Variable Stars, Rotation, Convective Boundaries, and Energy Conservation. *The Astrophysical Journal Supplement Series, 243*(1), 10.

SciPy. (n.d.). *Python Integration*. (Python) Retrieved July 1, 2021, from https://docs.scipy.org/doc/scipy/reference/generated/scipy.integrate.quad.html

Townsend, R. H., & Teitler, S. (2013). GYRE: An open-source stellar oscillation code based on a new Magnus Multiple Shooting scheme. *Monthly Notices of the Royal Astronomical Society, 435*(4), 3406-3418.

Weinberg, N. N., Arras, P., Quataert, E., & Burkart, J. (2012). Nonlinear Tides in Close Binary Systems. *The Astrophysical Journal, 751*(2), 136.

[redacted] Appendix

```
&star_job

    show_log_description_at_start = .false.

    load_saved_model = .true.
    saved_model_name = 'start.mod'

    save_model_when_terminate = .true.
    save_model_filename = 'end_core_h_burn.mod'
    required_termination_code_string = 'xa_central_lower_limit'


    change_D_omega_flag = .true.
    new_D_omega_flag = .true.


    !pgstar_flag = .true.

/ ! end of star_job namelist

&eos
```

```
/ ! end of eos namelist

&kap
      Zbase = 0.02d0

      kap_file_prefix = 'gs98'
      use_Type2_opacities = .true.

/ ! end of kap namelist

&controls

      write_pulse_data_with_profile = .true.
      pulse_data_format = 'GYRE'

      xa_central_lower_limit_species(1) = 'h1'
      xa_central_lower_limit(1) = 0.0001

      use_dedt_form_of_energy_eqn = .true.

      num_trace_history_values = 2
      trace_history_value_name(1) = 'rel_E_err'
      trace_history_value_name(2) = 'log_rel_run_E_err'
```

```
! limit max_model_number as part of test_suite
max_model_number = 2000

initial_mass = 1.0
initial_z = 0.02d0

max_center_cell_dq = 1d-14

! R_function = R_function_weight*log10(1 + (r/Rsun)/R_function_param)
R_function_weight = 300
R_function_param = 1d-9

am_nu_visc_factor = 0
am_D_mix_factor = 0.0333333333333333d0
D_DSI_factor = 0
D_SH_factor = 1
D_SSI_factor = 1
D_ES_factor = 1
D_GSF_factor = 1
D_ST_factor = 1

varcontrol_target = 1d-3
delta_lgL_He_limit = 0.01d0
```

```
      cool_wind_full_on_T = 9.99d9
      hot_wind_full_on_T = 1d10
      cool_wind_RGB_scheme = 'Reimers'
      cool_wind_AGB_scheme = 'Blocker'
      RGB_to_AGB_wind_switch = 1d-4
      Reimers_scaling_factor = 0.8d0
      Blocker_scaling_factor = 0.7d0 ! 0.8d0

      photo_interval = 50
      profile_interval = 1
      history_interval = 10
      terminal_interval = 10
      write_header_frequency = 10


/ ! end of controls namelist



&pgstar



      Grid6_win_flag = .true.
```

```
            Grid6_win_width = 11


            !Grid6_file_flag = .true.
            Grid6_file_dir = 'png'
            Grid6_file_prefix = 'grid6_'
            Grid6_file_interval = 5 ! output when
mod(model_number,Grid6_file_interval)==0
            Grid6_file_width = -1 ! (inches) negative means use same value as for
window
            Grid6_file_aspect_ratio = -1 ! negative means use same value as for window


            Summary_Burn_xaxis_name = 'mass'
            Summary_Burn_xaxis_reversed = .false.
            Summary_Burn_xmin = 0.00 ! -101d0 ! only used if /= -101d0
            Summary_Burn_xmax = 2.1  ! only used if /= -101d0


            Abundance_xaxis_name = 'mass'
            Abundance_xaxis_reversed = .false.
            ! power xaxis limits -- to override system default selections
            Abundance_xmin = 0.00 ! -101d0 ! only used if /= -101d0
            Abundance_xmax = -101d0 ! only used if /= -101d0
            Abundance_log_mass_frac_min = -6 ! only used if < 0


            !Profile_Panels4_win_flag = .true.
            !Profile_Panels4_win_width = 6
```

```
! Abundance window -- current model abundance profiles

   !Abundance_win_flag = .true.

   Abundance_win_width = 9
   Abundance_win_aspect_ratio = 0.75 ! aspect_ratio = height/width

/ ! end of pgstar namelist
```

Biographical Information

Niyousha Davachi studied Mathematics and Physics and earned her two Bachelor of Science degrees in 2019 from the University of Texas at Arlington. As an undergraduate, she began doing research in theoretical physics under the guidance of Dr. Zdzislaw Musielak, which lead to her finding interest in astrophysics and exoplanets. She then focused on hot Jupiter systems under the guidance of Dr. Nevin Weinberg and earned her Master of Science in Physics in 2021 from the University of Texas at Arlington.